Environmental Science & Technology

pubs.acs.org/est

Article

Cr(VI) Reduction and Sequestration by FeS Nanoparticles Formed in situ as Aquifer Material Coating to Create a Regenerable Reactive Zone

Zhenhai Liu, Qihong Yang, Panpan Zhu, Yaqi Liu, Xin Tong, Tianchi Cao, Mason B. Tomson, Pedro J. J. Alvarez, Tong Zhang,* and Wei Chen

Cite This: *Environ. Sci. Technol.* 2024, 58, 7186−7195

Read Online

ACCESS | Metrics & More | Article Recommendations | Supporting Information

ABSTRACT: Remediation of large and dilute plumes of groundwater contaminated by oxidized pollutants such as chromate is a common and difficult challenge. Herein, we show that in situ formation of FeS nanoparticles (using dissolved Fe(II), S(-II), and natural organic matter as a nucleating template) results in uniform coating of aquifer material to create a regenerable reactive zone that mitigates Cr(VI) migration. Flow-through columns packed with quartz sand are amended first with an Fe^{2+} solution and then with a HS^- solution to form a nano-FeS coating on the sand, which does not hinder permeability. This nano-FeS coating effectively reduces and immobilizes Cr(VI), forming Fe(III)−Cr(III) coprecipitates with negligible detachment from the sand grains. Preconditioning the sand with humic or fulvic acid (used as model natural organic matter (NOM)) further enhances Cr(VI) sequestration, as NOM provides additional binding sites of Fe^{2+} and mediates both nucleation and growth of FeS nanoparticles, as verified with spectroscopic and microscopic evidence. Reactivity can be easily replenished by repeating the procedures used to form the reactive coating. These findings demonstrate that such enhancement of attenuation capacity can be an effective option to mitigate Cr(VI) plume migration and exposure, particularly when tackling contaminant rebound post source remediation.

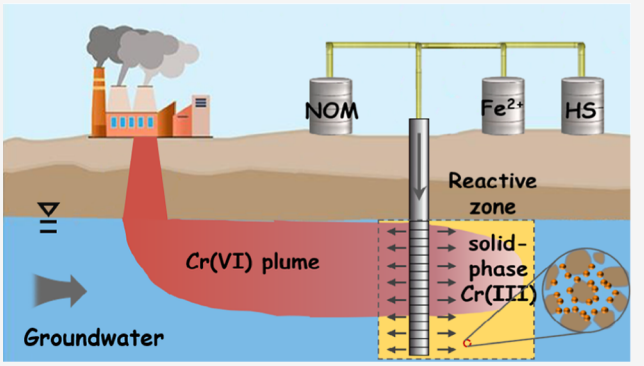

KEYWORDS: *FeS nanoparticles, permeable reactive barrier, reactive zone, plume control*

INTRODUCTION

Hexavalent chromium [Cr(VI)] is one of the most commonly detected metal contaminants in groundwater.[1,2] Approximately 11% of the polluted sites on the U.S. National Priorities List are contaminated by Cr(VI),[3] and persistence of Cr(VI) contamination at concentrations above the maximum contaminant level (MCL) is common, even after decades of remediation.[1,2,4] Cost-effective management of long-term contamination of groundwater at low concentrations is particularly challenging.[4−8] Most of the remedial technologies designed for fast removal of Cr(VI) (e.g., in situ precipitation or chemical reduction) are less efficient for lasting large plumes of low contaminant concentrations.[9−15] Permeable reactive barriers have been used, and yet the loss of permeability due to biofouling or mineral precipitation limits their applicability.[16,17] Currently, pump and treat is still the most commonly used approach in dealing with low-level residual Cr(VI) at many contaminated sites, but the generation of large quantities of wastewater and the long-term operating costs hinder its feasibility.[18,19]

One potential solution to dilute Cr(VI) plumes is modifying the aquifer materials in situ to enhance their reactivity toward Cr(VI). For example, coating aquifer materials with a thin layer of FeS nanoparticles may endow an aquifer with long-lasting capability to immobilize Cr(VI), by converting Cr(VI) to insoluble and nontoxic Cr(III) and preventing it from migrating downgradient. One significant advantage of this approach is that it can be easily implemented to create a reactive zone of the desired size, either used to treat a whole plume or placed as a permeable reactive barrier to mitigate Cr(VI) migration. The use of soluble constituents as precursors also overcomes the challenges of evenly distributing nanoparticles in aquifers. Two previous studies showed that flushing quartz sand-packed columns alternatively with an

Received: December 16, 2023
Revised: March 28, 2024
Accepted: March 29, 2024
Published: April 10, 2024

$FeSO_4$ and a Na_2S solution resulted in the formation of FeS aggregates, which were able to remove a fraction of the inflow As(III).[20,21] For example, over 80% of As(III) (initial concentration of 1 mg/L) was sequestered in the beginning stage [up to approximately 23 pore volumes (PV)], and the As removal capacity was not saturated until 216 PV.[20] The key to the successful deployment of this remedial strategy is maintaining the reactivity and efficacy of the nano-FeS coating (that is, Cr(VI) concentrations in the reactive zone need to be well below the MCL for months or longer) while minimizing the impact on permeability and groundwater flow regime (so that the reactivity of the porous media can be replenished by repeatedly coating the sand grains). This can probably be done by modulating the precipitation process (e.g., sizes and distributions of FeS nanoparticles on sand grains) using natural macromolecules as templates.

Here, we prove the concept that coating sand grains in situ with FeS nanoparticles can be an effective measure to control chromium contamination at low concentrations. Nano-FeS coatings were formed by flushing columns packed with quartz sand sequentially with $FeSO_4$ and Na_2S solutions, and the mass, sizes, and distribution of the FeS nanoparticles were modulated by preconditioning the sand with Suwannee River humic acid (HA) or fulvic acid (FA). The efficacy of the reactive coatings was examined using column experiments by measuring breakthrough profiles of Cr(VI) and characterizing the reduction and precipitation products. The roles of HA/FA in modulating the dynamics of nucleation and particle growth were examined with in situ grazing incidence small-angle X-ray scattering (GISAXS) and atomic force microscopy (AFM), as well as quartz crystal microbalance with dissipation (QCM-D), excitation−emission matrix (EEM), and two-dimensional correlation spectroscopy. The viability of forming a fresh nano-FeS coating on the spent sand grains was demonstrated. These findings demonstrate that such an enhancement of the attenuation capacity of aquifer material can be a practical plume management option.

MATERIALS AND METHODS

In Situ Formation of Nano-FeS Coating. FeS nanoparticles were allowed to form on quartz sand by alternately flushing the columns with an $FeSO_4$ solution (20 mM) and then a Na_2S (20 mM) solution for three cycles (Figure S1), after pre-equilibrating with artificial groundwater (detailed recipe in Table S1). Detailed procedures and parameters as well as measures taken to maintain anoxic conditions are summarized in Supporting Information and Table S2. To modulate the size and distribution of nano-FeS, 200 mL of a HA or FA solution (20 mg C/L) was flushed through a column, prior to initiating precipitation of FeS; the rest of the procedures were the same as above. After the formation of nano-FeS coating, the breakthrough curve of a conservative tracer (KBr, 100 mg/L) was obtained to assess the porosity of the columns. The distribution of nano-FeS in the columns was determined by measuring the content of Fe in each of a 1 cm segment. The columns were then flushed with artificial groundwater at a pore velocity of 0.4 m/d to test the stability of an in situ formed nano-FeS coating on quartz sands. Detailed characterizations of the nano-FeS coating are given in Supporting Information.

Cr(VI) Sequestration Experiments. A K_2CrO_4 solution (0.5 mg/L) in artificial groundwater was injected into the sand columns at a pore velocity of 0.4 m/d. Effluent samples were collected periodically (every ∼7.2 PV) and the concentrations of Cr(VI) and Cr(III) were measured. Injection of the K_2CrO_4 solution was stopped once a complete breakthrough of Cr(VI) was reached. The changes in pH and redox potential were monitored during the time course of the experiments, and the fluctuation was insignificant (Figure S2). The viability to replenish the reactivity of a spent column was tested by repeating the nano-FeS coating formation procedures, using the HA-pretreated columns after complete breakthrough of Cr(VI) was reached. Then, Cr(VI) sequestration experiments were carried out using these columns. The dimensionless retardation factor (R) was calculated based on the breakthrough curves (see Supporting Information for detailed calculation).[20] To evaluate the stability of sequestered Cr, selected columns were flushed with K_2CrO_4-free artificial groundwater at the end of the Cr-sequestration experiments, and the concentrations of Cr in the effluent were determined. The analytical procedures for aqueous and solid-phase samples are given in Supporting Information.

Spectroscopic Analyses. Three-dimensional EEM (3D-EEM) fluorescence spectroscopy (F-7100, Hitachi) was used to quantitatively characterize the binding between NOM and Fe^{2+} by analyzing the change in fluorescence intensity of the NOM samples before and after reacting with Fe^{2+}. The fluorescence spectra were collected at 5 nm increments with a scan speed of 12 000 nm/min. The range of the scanning wavelength was set at 200−450 nm for excitation and 250−550 nm for emission. The two-dimensional (2-D) correlation spectra were obtained from Fourier transform infrared spectroscopy (FTIR, Tensor 27, Bruker Optics Inc.) within the range of 4000−400 cm^{-1} at a resolution of 4 cm^{-1}. The spectral data were processed using Shi 2.0 software.

In Situ GISAXS Measurement. GISAXS measurements were carried out at beamline BL16B1 of the Shanghai Synchrotron Radiation Facility, using a Pilatus 2 M area detector. A flat quartz with an exposed (110) surface (10 × 10 × 1 mm) was selected as the substrate for heterogeneous precipitation. Organic-coated substrates were prepared using a method reported in the literature.[22−24] Before each measurement, a quartz substrate was placed in a specially designed GISAXS cell parallel to the X-ray beam. The operation energy was 10 keV and the incident angle was 0.05°. The Fe^{2+} and HS^- solutions were prepared on-site in a disposable glovebox and were then injected into the GISAXS cell. The camera exposure time was set to 120 s for collecting the scattering images. All GISAXS data were corrected using the background scattering spectra. The two-dimensional scattering images were integrated to obtain the one-dimensional GISAXS intensity, $I(q)$, as a function of scattering vector (q), using the Fit2D v10.132 software. The parameter q was estimated as $q = 4\pi \times (\sin\theta)/\lambda$, where λ is the wavelength of X-ray and 2θ is the scattering angle.[25]

AFM Measurement. FeS nanoparticles formed on quartz surfaces were also characterized with AFM (Bruker, Dimension Icon). AFM tapping mode was operated at a scan rate of 0.988 Hz. AFM probes (silicon tips, TESPA, Brukerprobes) were 115 μm in length and 25 μm in width without an extra coating on the front side. The peak force frequency was 2 kHz, and the typical spring constant was 40 N/m. The height, amplitude, and phase images were collected simultaneously. When evaluating the effect of NOM on heterogeneous nucleation and growth of nano-FeS, multiple scan spots of different samples were measured to confirm completely uniform

https://doi.org/10.1021/acs.est.3c10637
Environ. Sci. Technol. 2024, 58, 7186−7195

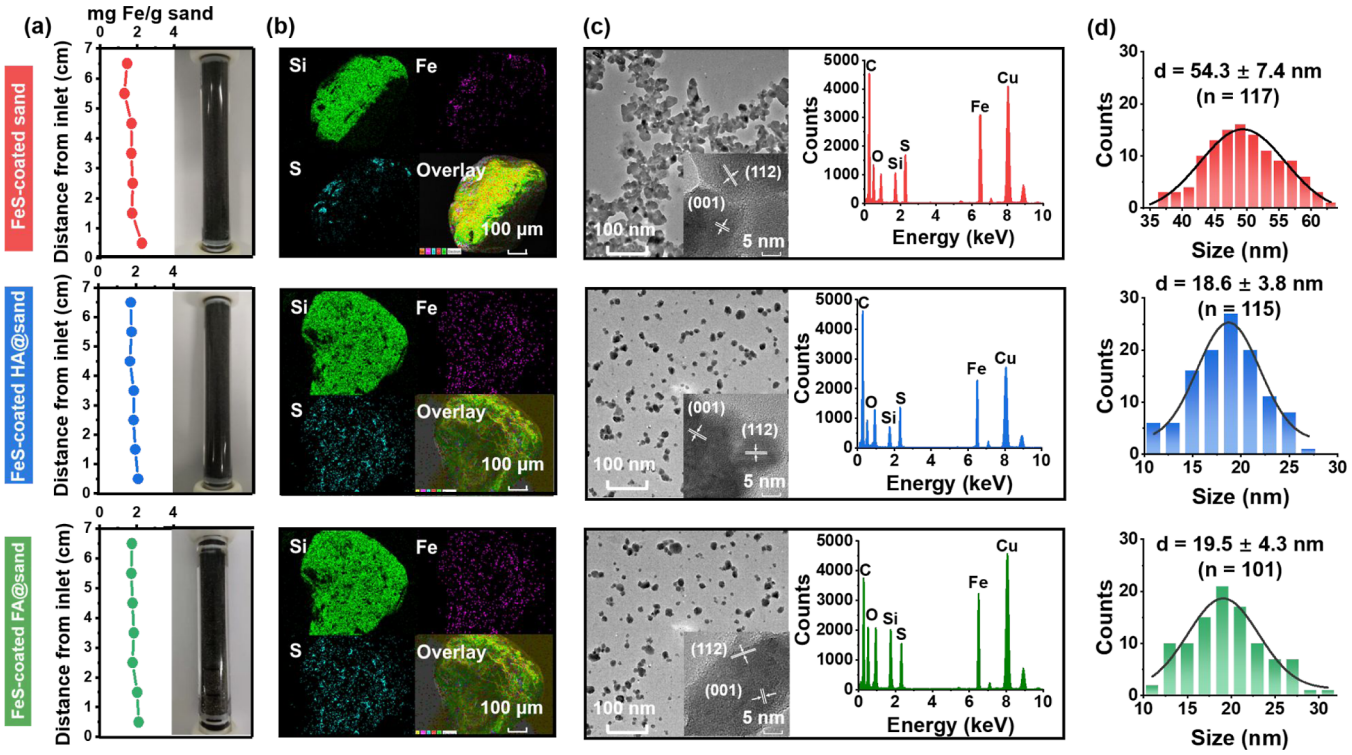

Figure 1. Distribution of Fe along the columns as shown by the measured Fe contents and photographs of the columns (a), elemental mapping images of sand grains (b), TEM images and EDX spectra of FeS nanoparticles (c), and particle size distribution of FeS nanoparticles (d), showing the formation of nano-FeS coating on sand grains and preconditioning a column with humic or fulvic acid facilitates the formation of smaller-sized nanoparticles that are more uniformly distributed along the columns. The inset in the TEM images is the HR-TEM images. Particle size distribution is obtained by measuring more than 100 particles (detached from the sand grains by ultrasonication) from TEM images using ImageJ processing software. HA@sand and FA@sand indicate that sand received humic and fulvic acid pretreatment prior to initiating FeS precipitation.

coverage of NOM on the quartz surfaces prior to the addition of Fe^{2+} and HS^- solutions (Figure S3). NanoScope Analysis 1.8 software was used to analyze the collected images and topographic information on the samples.

QCM-D Measurement. The real-time deposition and viscoelastic properties of FeS nanoparticles were examined using a QCM-D (Q-Sense Explorer, Biolin Scientific AB), and crystal sensors coated with silica (SiO_2, QSX303) were employed. The shifts in frequency (Δf) and energy dissipation (ΔD) were simultaneously monitored. The flow rate of all solutions was kept constant at a rate of 0.1 mL/h, and the temperature was maintained at 25 ± 0.2 °C throughout the experiments. In the beginning of a QCM-D experiment, deionized water was flowed through the QCM-D chamber until a stable signal baseline of Δf and ΔD responses was equilibrated. Afterward, an Fe^{2+} solution and then a HS^- solution were passed through the chamber for a total duration of 30−40 min. Finally, deionized water was flowed through the chamber again, until the signals of Δf and ΔD became stable. For the experiments involving NOM, the SiO_2 sensors were first coated with NOM solution (20 mg C/L) for 40 s using a spin coater at a speed of 8000 rpm. The sensors were then air-dried, followed by complete drying in the vacuum.

RESULTS AND DISCUSSION

Nano-FeS Coating Formed *In Situ* by Flushing Porous Media In Tandem with Fe^{2+} and HS^- Can Effectively Sequester Cr(VI). Under anoxic conditions, flushing the columns packed with quartz sand alternately with an $FeSO_4$ solution and then with a Na_2S solution can form a layer of FeS nanoparticles on the sand grains. The distribution of FeS along the column was relatively uniform, with the mass of FeS slightly higher near the inlet (Figure 1a). The elemental mapping of iron and sulfur (Figure 1b), as well as the scanning electron microscopy (SEM) and energy dispersive X-ray spectroscopy (EDX) results (Figure S4), confirmed that FeS evenly covered the sand grains. The transmission electron microscope (TEM; Figure 1c) and AFM images (Figure S5) revealed that the sizes of the FeS precipitates were within the nanorange and followed a normal distribution (Figure 1d). The specific surface area of the sand grains significantly increased upon coating with FeS nanoparticles (Figure S6). The powder X-ray diffraction (XRD) spectra demonstrated that the nanoparticles were mackinawite (FeS, JCPDS: 15-0037; Figure S7), and the high-resolution TEM (HR-TEM) images (Figure 1c) showed that (001) and (112) were the predominantly exposed facets. Furthermore, X-ray photoelectron spectroscopy (XPS) confirmed Fe(II) and S(-II) as the main species (Figure S8). The coating of the FeS nanoparticles had negligible effects on the porosity of the columns, indicated by the overlapping breakthrough curves of KBr before and after FeS formation (Figure S9).

In situ formation of the nano-FeS coating significantly enhanced the capability of the porous medium to reduce and sequester Cr(VI). Complete breakthrough of Cr(VI) from the columns packed with bare sand was observed after only 2 PV, whereas no breakthrough of Cr(VI) (the concentrations were below the detection limit) was observed for the columns containing nano-FeS-coated sand until 654 PV (Figure 2a). The calculated retardation factor (R_{Cr}) increased from 3 for

https://doi.org/10.1021/acs.est.3c10637
Environ. Sci. Technol. 2024, 58, 7186−7195

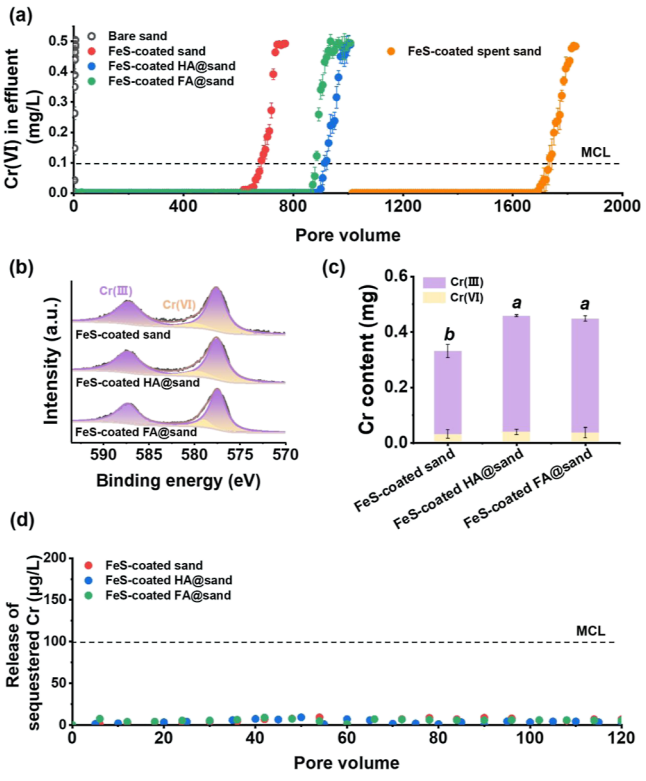

Figure 2. Breakthrough curves of Cr(VI), showing that the in situ formed nano-FeS coating can effectively sequester Cr(VI), and pretreating sand with humic or fulvic acid prior to initiating FeS precipitation further enhances the ability of the nano-FeS coating in sequestering Cr(VI) (a). Cr 2p XPS spectra of Cr-laden sand (b) and mass of different Cr species on Cr-laden sand determined with ICP−MS analysis (c), showing most of the Cr(VI) sequestered in the columns has been converted to solid-phase Cr(III). Leaching of Cr from Cr-laden sand (d), showing negligible remobilization of sequestrated Cr. Concentration of Cr(VI) in the influent is 0.5 mg/L, and pore velocity is 0.4 m/d. Dotted line indicates maximum contaminant level (MCL, 0.1 mg/L) of Cr. Values that are statistically different ($p < 0.05$) according to the one-way analysis of variance (ANOVA) are indicated by italic lowercase letters.

the bare sand to 1031 for the FeS-coated sand (Figure S10), and the coexisting constituents in the synthetic groundwater did not apparently impede the sequestration of Cr(VI), even at concentrations much higher than that of Cr(VI). The Cr 2p XPS spectra showed that most of the Cr on the sand grains was in the form of solid-phase Cr(III) (Figure 2b), and the ICP−MS analysis corroborated that Cr(III) accounted for more than 90% of the total Cr sequestered in the columns (Figure 2c). The Fe 2p and S 2p XPS spectra of the sand grains showed the conversion of Fe(II) to Fe(III), and S(-II) to S_{oxi} (e.g., polysulfide, sulfite, or sulfate, Figure S11).[26−28] Note that to shorten the experimental duration, a relatively high pore velocity of 0.4 m/day was used in this study. Even at this velocity, the effluent concentration of Cr(VI) was well below the MCL until 680 PV, corresponding to approximately two months of flushing. Thus, it is reasonable to conclude that in situ formed FeS coating likely remains effective for Cr(VI) sequestration for a prolonged period of time.

Nano-FeS Coating Distribution and Performance Were Enhanced by Modulating Heterogeneous Nucleation and Nanoparticle Growth Using Natural Organic Matter. To enhance the efficacy of the nano-FeS coating in sequestering Cr(VI), we pretreated the sand grains with HA and FA (as model NOM) to modulate the formation processes of the nanoparticles. This resulted in the formation of larger amounts of smaller FeS nanoparticles (Figure S12) while having negligible effects on the crystalline phase and planes of nano-FeS (Figures 1c and S7). Specifically, the mass distribution of FeS nanoparticles inside the columns was more even compared with the columns receiving no NOM pretreatment (see the much flatter profiles of Fe distribution along the columns in Figure 1a). The elemental mapping results showed that a larger amount of FeS nanoparticles were formed on the sand grains (Figure 1b). This was confirmed by the measured mass of FeS formed on the HA/FA-pretreated sand (9.24 and 9.52 mg, respectively) vs that on the bare sand (8.12 mg; $p < 0.05$). With NOM pretreatment the sizes of the FeS nanoparticles were markedly reduced, from an average diameter of 54.3 nm on the bare sand to 18.6 and 19.5 nm on the HA- and FA-pretreated sand (Figure 1d). The specific surface areas of the FeS-coated sand grains were 2.49 m^2/g for HA-pretreated sand and 2.42 m^2/g for FA-pretreated sand, compared with 1.81 m^2/g for the sand receiving no NOM pretreatment (Figure S6). As expected, the nano-FeS coatings formed on the HA/FA-pretreated sand were much more effective in sequestering Cr(VI) than those formed on bare sand (Figure 2a,c). The earliest breakthrough of Cr was not observed until 902 and 872 PV, respectively, a 33−38% increase in Cr-sequestering efficacy. The mass of Cr(VI) sequestered per unit mass of FeS was 51.2 and 48.1 mg/g for the FeS nanoparticles formed on the HA and FA-pretreated sand, higher than the value of 41.0 mg/g when no NOM pretreatment was involved (Figure S13). (These Cr(VI)-sequestering capabilities are comparable to or higher than those reported in the literature for suspended FeS nanoparticles.[26,29]) A previous study showed that Cr(VI) was reduced by HA-Fe(II) complexes in anoxic porewater, forming Fe(III)−Cr(III) (oxyhydr-)oxide particles with a size distribution dependent on HA concentration.[30] Similar products were formed in the columns pretreated with HA or FA, further demonstrating the effectiveness of the in situ formed nano-FeS coating in removing and reducing Cr(VI).

Two advantages can be gained by preconditioning the columns with NOM. First, the adsorption of NOM to the sand grains provides additional binding sites for Fe^{2+} and subsequently facilitates the heterogeneous nucleation of FeS. Second, NOM macromolecules serve as templates for controlling the growth and stabilizing the aggregation of FeS nanoparticles.[22] For the sand grains receiving no HA/FA pretreatment, the main binding sites for Fe^{2+} were the surface −OH groups of SiO_2.[22] These silanol groups can bind Fe^{2+} via the formation of Fe−O−Si complexes,[22,31] as demonstrated with FTIR and XPS analyses.[32,33] Coating of NOM can markedly increase the abundance of Fe^{2+}-binding sites, as NOM is rich in Fe-complexing groups, such as −COOH, −OH, and $-NH_2$.[34,35] Fluorescence quenching experiments demonstrated the chemical complexation between HA/FA and Fe^{2+} (Figure 3a,b). Two prominent peaks were identified from the 3D-EEM of HA and FA at excitation/emission (E_x/E_m) wavelength of 265/450 nm (peak A) and 325/450 nm (peak B), corresponding to fulvic-acid like and humic-acid like substances, respectively.[36,37] The fluorescence intensities of both substances diminished by over 90% after Fe^{2+} was added to the HA or FA solution (Figure 3c,d). The synchronous map generated from the FTIR data exhibits two main auto peaks at

https://doi.org/10.1021/acs.est.3c10637
Environ. Sci. Technol. 2024, 58, 7186−7195

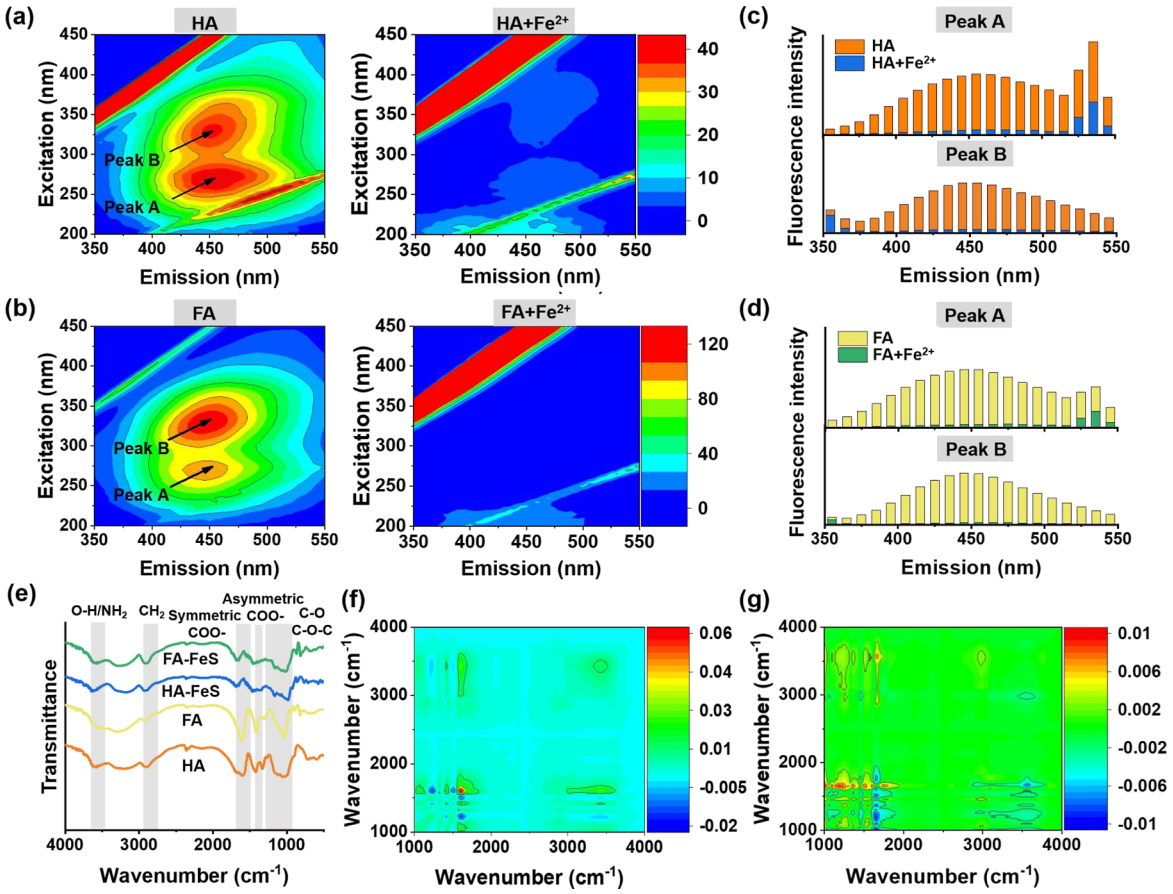

Figure 3. 3D-EEM fluorescence spectra of humic acid (a) and fulvic acid (b) before and after reacting with Fe^{2+}, and histograms of fluorescence quenching at excitation wavelengths of peak A and peak B of humic acid (c) and fulvic acid (d) induced by Fe^{2+}, showing the strong complexation between humic acid/fulvic acid and Fe^{2+}. FTIR spectra (e) and synchronous (f) and asynchronous (g) 2D correlation maps generated from the 4000−1000 cm^{-1} regions of the FTIR spectra, showing the relative binding strength of different functional groups of humic/fulvic acid toward Fe^{2+}. Positive and negative correlations are indicated by red and blue color, respectively, and correlation strength is proportional to color intensity.

the 1635 and 3400 cm^{-1}, as well as a positive and two negative cross-peaks centered at the wavenumber pairs of 3400/1635, 3400/1230, and 1635/1230 cm^{-1} (Figure 3e,f). These results show that −COOH (1635 cm^{-1}), −OH and possibly $-NH_2$ (3400 cm^{-1}), and C−O (1230 cm^{-1}) were responsible for the binding of Fe^{2+} to HA/FA.[35] Additionally, three negative cross-peaks were observed on the asynchronous map with wavelength pairs of 3400/1635, 3400/1230, and 1635/1230 cm^{-1} (Figure 3e,g). The comparison of the cross-peaks on the synchronous and asynchronous maps indicated that the relative binding strength for Fe^{2+} followed the order of −COOH > $-OH/-NH_2$ > C−O.

The GISAXS analysis helps explain the effects of NOM pretreatment on the nucleation, growth, and aggregation of FeS nanoparticles. In a typical GISAXS 1D spectrum, the trend of scattering intensity, $I(q)$, in the high-q range corresponds to particle growth, while that in the low-q range corresponds to particle−particle agglomeration.[28,38−41] In both the high-q and low-q ranges, the $I(q)$ values of the nanoparticles formed on the surfaces receiving no HA/FA pretreatment went up with time (Figure 4a), indicating the increase of particle sizes and the increase of particle−particle agglomeration. In comparison, the $I(q)$ values of the nanoparticles formed on HA- and FA-pretreated surfaces changed little (Figure 4c,e). Additionally, the $I(q)$ values are also markedly lower for the nanoparticles formed on HA/FA-pretreated surfaces (Figure 4a,c,e), indicating that the initially formed nuclei (i.e., the monomers) were of smaller sizes and the subsequent formation of agglomerates was slower.[42] The AFM images (Figure 4b,d,f) of the FeS nanoparticles formed on quartz surfaces corroborated the GISAXS results, in that the FeS nanoparticles formed on HA- or FA-pretreated surfaces were much smaller in size and much more uniform in size distribution. Coating of sand grains with HA or FA increased their hydrophobicity (as indicated by the higher contact angles, 16.1 and 15.3° for the HA and FA-pretreated sand, vs 3.9° for the bare sand; Figure S14). According to the classical nucleation theory, surfaces with greater hydrophobicity have higher substrate−solution interfacial energy, resulting in lower energy barrier for heterogeneous nucleation and consequently, faster nucleation rate and smaller initial nuclei sizes.[25,43−47] Moreover, the presence of NOM increased the steric hindrance and possibly electrostatic repulsion (Figure S15) between the initially formed FeS nanoparticles, thus, inhibiting particle agglomeration.[30,48−50] Thus, the GISAXS and AFM data collectively indicated that preconditioning with HA and FA affected both the monomer size and the aggregate structures of the FeS nanoparticles.

Nano-FeS Coating Stays Attached to Sand Grains during Cr(VI) Removal and Can Be Easily Replenished. We observed minimal detachment of the FeS nanoparticles from the sand grains regardless of whether NOM pretreatment

https://doi.org/10.1021/acs.est.3c10637
Environ. Sci. Technol. 2024, 58, 7186−7195

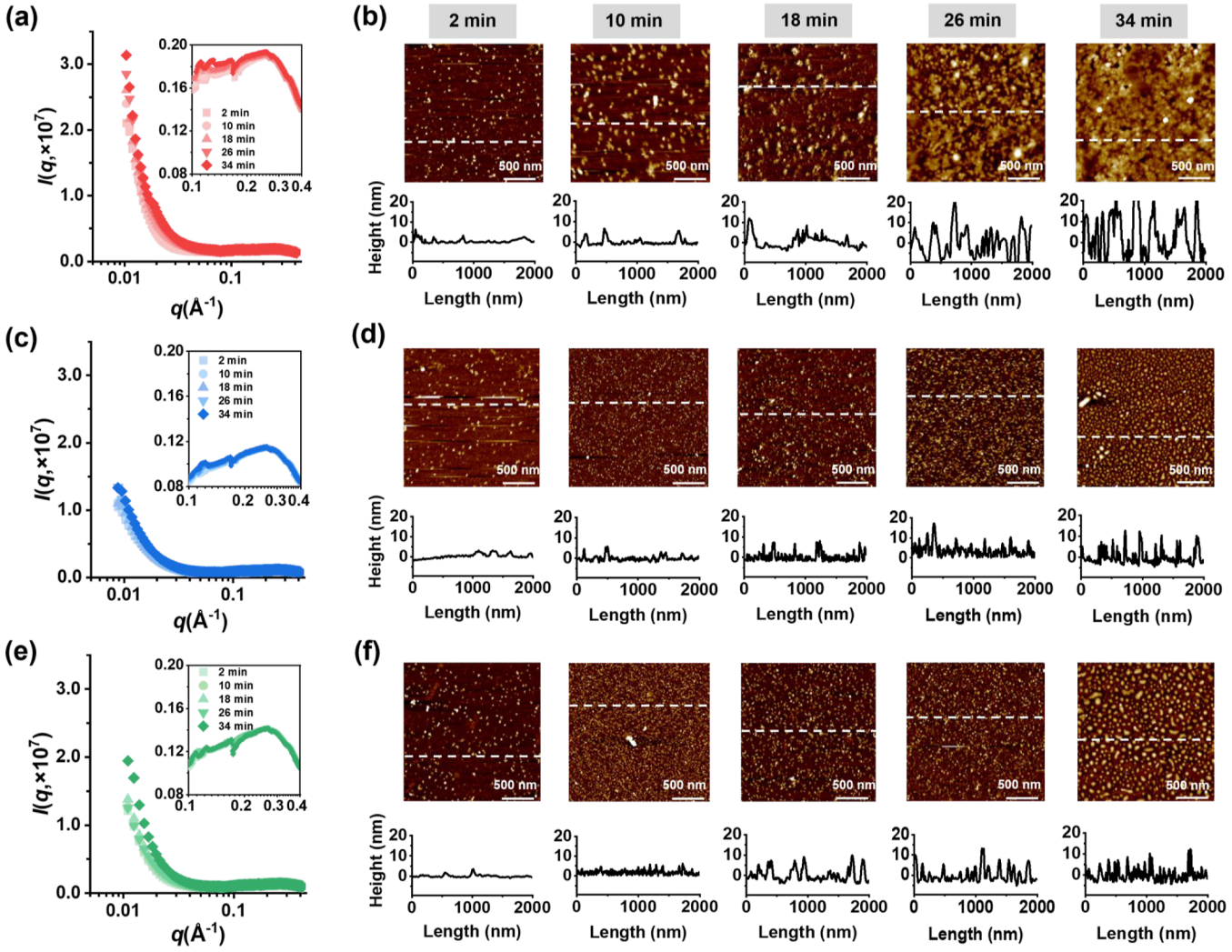

Figure 4. Representative GISAXS 1D scattering intensity (a,c,e) and AFM images (b,d,f) of FeS nanoparticles on quartz surface in the absence (a,b) and presence of humic acid (c,d) or fulvic acid (e,f) at different time points during precipitation, showing the presence of natural organic matter decreases the sizes of initial nuclei and inhibits agglomeration of FeS. The insets in figures (a,c,e) show the scattering intensity of FeS nanoparticles in the high-q ranges. Height cross sections taken across the white dotted line in each AFM image (b,d,f) are given below its corresponding image.

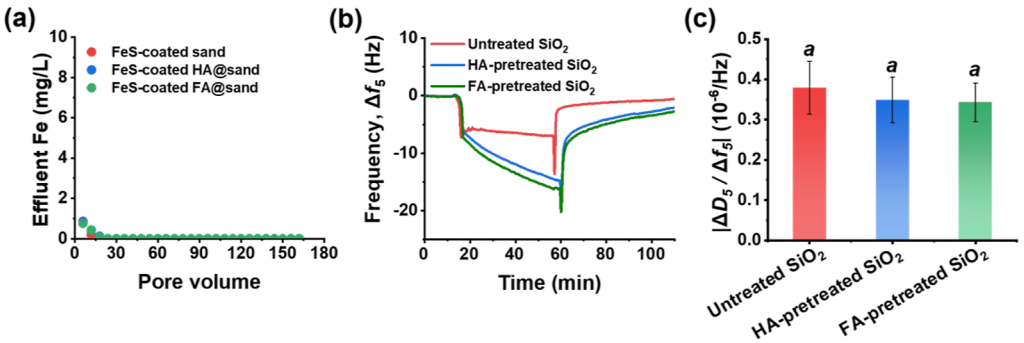

Figure 5. Effluent Fe concentration in column flushing experiments after the formation of nano-FeS coating on sand surfaces (a), showing that FeS nanoparticles are tightly bound to sand grains with limited detachment. Representative normalized frequency shift (Δf) for the deposition of FeS on SiO_2-coated sensors (b) and the ratio of dissipation (ΔD) to Δf ($|\Delta D_5/\Delta f_5|$) for nano-FeS deposition (c), showing humic/fulvic acid pretreatment increases the mass of FeS precipitated but does not affect the morphology of FeS nanoparticles on the sand.

was applied. Flushing the columns with Cr-free synthetic groundwater (160 PV in total) after forming the nano-FeS coating resulted in the detachment of only 0.2−0.3% of total Fe (Figure 5a). The concentrations of Fe in the effluents were also monitored in the Cr-removal experiments and were below the detection limit throughout the experiments (Figure S16). The even lesser degree of detachment of Fe after FeS reacted with Cr(VI) was likely attributed to the formation of Cr(III)−

https://doi.org/10.1021/acs.est.3c10637
Environ. Sci. Technol. 2024, 58, 7186−7195

Fe(III) mineral phases (Figures 2b and S11).[32,51] No noticeable differences in iron release were observed between the HA/FA-pretreated sand and the sand receiving no NOM pretreatment. The strong attachment of the FeS nanoparticles to the sand grains ensured the sustainable sequestration of Cr. Indeed, flushing the Cr-saturated columns with Cr-free synthetic groundwater (120 PV) remobilized less than 0.1% of sequestered Cr, and the total Cr concentrations in the effluent were only 1.1−9.2% of the MCL (Figure 2d).

The structures, particularly the viscoelastic properties, of the FeS coating formed on the surface of the sand grains were further assessed on a QCM-D instrument by recording the real-time deposition processes. Preconditioning the SiO_2 sensor with HA or FA resulted in more significant frequency shifts, in line with that a greater mass of FeS deposited onto the sensor (Figure 5b). However, the $|\Delta D/\Delta f|$ values associated with HA/FA-pretreated and nontreated sensors were statistically undistinguishable ($p > 0.05$, Figure 5c), and were all well below 1×10^{-6}/Hz, a threshold below which the adsorbed layer structure is assumed to be relatively rigid, compact, and evenly distributed, whereas larger $|\Delta D/\Delta f|$ values indicate soft and loosely bound structures.[52−56]

The viability of replenishing the Cr-sequestering capability of porous media was verified by coating the spent sand (i.e., after the sand was no longer able to detain Cr(VI) flushed into the columns) with a fresh layer of FeS nanoparticles. The newly formed layer exhibited similar Cr-removal capability of the previous one, being able to sequester Cr(VI) up to 720 PV (the calculated R_{Cr} value is 1022, Figure 2a), while having no effect on the porosity of the column (Figure S9). A supplementary experiment carried out using influents of higher initial Cr(VI) concentration (5 mg/L) showed that the performance was consistent even after 8 cycles of recoating with nano-FeS (Figure S17). These results show that the contaminant-sequestering capability of an aquifer can be retained by periodically repeating the nano-FeS formation process. An additional benefit of this replenishing method is that the newly formed layer may help further incapsulate the Cr sequestered by the previous layer.

Environmental Implications. Cost-effective management and remediation of large and dilute, persistent groundwater contaminant plumes remain a significant challenge to risk reduction at many impacted sites. Many approaches that have been developed for the fast removal of the bulk of contaminants at or near source zones (e.g., in situ precipitation or chemical reduction) often become much less efficient when the contaminant concentration is low and slow diffusion into porewater is a rate-limiting step of contaminant removal, as the operational and maintenance costs will be extremely high. Our study demonstrates that modifying aquifer porous media in situ with a coating of reactive nanoparticles can be a viable and scalable approach to ensuring long-term compliance. An important advantage of the concept of reactive zone over conventional reactive barriers (e.g., permeable reactive barriers using fillings such as zerovalent iron) is that it incurs little alteration to the hydrogeological settings of a site and, thus, has minimal interference on the flow fields and contaminant transport routes. Moreover, this approach is highly flexible and can be used to treat either the entire plume or part of a plume or simply laid out as a permeable reactive barrier to intercept the incoming pollutants. The use of dissolved species as the precursor compounds can overcome the mass transfer problems associated with moving nanoparticles in an aquifer and allows easy manipulation of solution chemistry to achieve desired mass, size, and distribution of the nanoparticle coating. (Note that relatively high concentrations of Fe(II) and S(-II) solutions were used to shorten the experimental duration; for field deployment, operational parameters such as injection doses, rate, frequency, and placing of injection points need to be carefully designed based on the specific geological settings, water chemistry conditions, and plume properties, to reduce the costs and minimize potential impact of excess and unbound Fe and S. Additional challenges such as biofilm formation on the coating, as well as oscillation of redox potential (e.g., due to the seasonal fluctuation of water table, or as the results of active remediation operations such as pumping), should be given special attention during remedial design for optimized performance. Moreover, while under the tested conditions of this study, S(-II) was converted largely to solid-phase polysulfide, sulfite, and sulfate, the potential impact of remobilization of these species and release of soluble S (e.g., sulfate ions) should be assessed based on site-specific conditions.) The conceptual model demonstrated in this study can be extended to the in situ formation of other reactive nanoparticles (e.g., hydrous ferric oxide, magnetite, gibbsite, and manganese dioxide), and is particularly suited as the polishing step of site remediation and for tackling post-remediation contaminant rebound.

■ ASSOCIATED CONTENT

Supporting Information

The Supporting Information is available free of charge at https://pubs.acs.org/doi/10.1021/acs.est.3c10637.

Additional experimental methods, and calculation of dimensionless retardation factor (R); tables summarizing recipes of artificial groundwater, parameters and protocols of column experiments, and selected properties of humic and fulvic acids; figures showing the procedures to form nano-FeS coating, effluent pH and ORP in column experiments, AFM, SEM, specific surface area, XRD, XPS, breakthrough curves of KBr, retardation factor, content of nano-FeS on quartz sand, dynamic retention capacity, contact angle, ζ potential, effluent Fe concentration during Cr(VI) sequestration, and Cr(VI) removal using replenished nano-FeS coatings (PDF)

■ AUTHOR INFORMATION

Corresponding Author

Tong Zhang − *College of Environmental Science and Engineering, Ministry of Education Key Laboratory of Pollution Processes and Environmental Criteria, Tianjin Key Laboratory of Environmental Remediation and Pollution Control, Nankai University, Tianjin 300350, China;* orcid.org/0000-0002-8151-3697; Phone: 86-22-2350-1117; Email: zhangtong@nankai.edu.cn; Fax: 86-22-2350-1117

Authors

Zhenhai Liu − *College of Environmental Science and Engineering, Ministry of Education Key Laboratory of Pollution Processes and Environmental Criteria, Tianjin Key Laboratory of Environmental Remediation and Pollution Control, Nankai University, Tianjin 300350, China*

https://doi.org/10.1021/acs.est.3c10637
Environ. Sci. Technol. 2024, 58, 7186−7195

Qihong Yang − *College of Environmental Science and Engineering, Ministry of Education Key Laboratory of Pollution Processes and Environmental Criteria, Tianjin Key Laboratory of Environmental Remediation and Pollution Control, Nankai University, Tianjin 300350, China*
Panpan Zhu − *College of Environmental Science and Engineering, Ministry of Education Key Laboratory of Pollution Processes and Environmental Criteria, Tianjin Key Laboratory of Environmental Remediation and Pollution Control, Nankai University, Tianjin 300350, China*
Yaqi Liu − *College of Environmental Science and Engineering, Ministry of Education Key Laboratory of Pollution Processes and Environmental Criteria, Tianjin Key Laboratory of Environmental Remediation and Pollution Control, Nankai University, Tianjin 300350, China*
Xin Tong − *College of Environmental Science and Engineering, Ministry of Education Key Laboratory of Pollution Processes and Environmental Criteria, Tianjin Key Laboratory of Environmental Remediation and Pollution Control, Nankai University, Tianjin 300350, China*
Tianchi Cao − *College of Environmental Science and Engineering, Ministry of Education Key Laboratory of Pollution Processes and Environmental Criteria, Tianjin Key Laboratory of Environmental Remediation and Pollution Control, Nankai University, Tianjin 300350, China*
Mason B. Tomson − *Department of Civil and Environmental Engineering, Rice University, Houston, Texas 77005, United States*
Pedro J. J. Alvarez − *Department of Civil and Environmental Engineering, Rice University, Houston, Texas 77005, United States;* orcid.org/0000-0002-6725-7199
Wei Chen − *College of Environmental Science and Engineering, Ministry of Education Key Laboratory of Pollution Processes and Environmental Criteria, Tianjin Key Laboratory of Environmental Remediation and Pollution Control, Nankai University, Tianjin 300350, China;* orcid.org/0000-0003-2106-4284

Complete contact information is available at: https://pubs.acs.org/10.1021/acs.est.3c10637

Notes

The authors declare no competing financial interest.

■ ACKNOWLEDGMENTS

This research was supported by the National Natural Science Foundation of China (22125603, 22020102004), Tianjin Municipal Science and Technology Bureau (21JCJQJC00060), and the Ministry of Education of China (T2017002). Partial funding for PJJA was provided by the NSF Nanosystems Engineering Research Center for Nanotechnology-Enabled Water Treatment (ERC-1449500). We thank beamlines BL16B1 of Shanghai Synchrotron Radiation Facility for providing the beam time.

■ REFERENCES

(1) U. S. Environmental Protection Agency. *In Situ Treatment of Soil and Groundwater Contaminated with Chromium (Technical Resource Guide), EPA 625/R-00/004*; US EPA, 2000.
(2) Zhang, P.; Van Nostrand, J. D.; He, Z.; Chakraborty, R.; Deng, Y.; Curtis, D.; Fields, M. W.; Hazen, T. C.; Arkin, A. P.; Zhou, J. A slow-release substrate stimulates groundwater microbial communities for long-term *in situ* Cr(VI) reduction. *Environ. Sci. Technol.* **2015**, *49*, 12922−12931.
(3) Shi, J.; Zhang, B.; Qiu, R.; Lai, C.; Jiang, Y.; He, C.; Guo, J. Microbial chromate reduction coupled to anaerobic oxidation of elemental sulfur or zerovalent iron. *Environ. Sci. Technol.* **2019**, *53*, 3198−3207.
(4) Faybishenko, B.; Hazen, T. C.; Long, P. E.; Brodie, E. L.; Conrad, M. E.; Hubbard, S. S.; Christensen, J. N.; Joyner, D.; Borglin, S. E.; Chakraborty, R.; Williams, K. H.; Peterson, J. E.; Chen, J. S.; Brown, S. T.; Tokunaga, T. K.; Wan, J. M.; Firestone, M.; Newcomer, D. R.; Resch, C. T.; Cantrell, K. J.; Willett, A.; Koenigsberg, S. *In situ* long-term reductive bioimmobilization of Cr(VI) in groundwater using hydrogen release compound. *Environ. Sci. Technol.* **2008**, *42*, 8478−8485.
(5) Sale, T.; Newell, C.; Stroo, H.; Hinchee, R.; Johnson, P. *Frequently Asked Questions Regarding the Management of Chlorinated Solvents in Soils and Groundwater*; Environmental Security Testing and Certification Program (ESTCP): Washington, DC, 2008.
(6) National Research Council. *Alternatives for Managing the Nation's Complex Contaminated Groundwater Sites*; National Academies Press, 2013.
(7) Stroo, H. F.; Leeson, A.; Marqusee, J. A.; Johnson, P. C.; Ward, C. H.; Kavanaugh, M. C.; Sale, T. C.; Newell, C. J.; Pennell, K. D.; Lebrón, C. A.; et al. Chlorinated ethene source remediation: Lessons learned. *Environ. Sci. Technol.* **2012**, *46*, 6438−6447.
(8) Meray, A.; Sturla, S.; Siddiquee, M.; Serata, R.; Uhlemann, S.; Gonzalez-Raymat, H.; Denham, M.; Upadhyay, H.; Lagos, L.; Eddy-Dilek, C.; Wainwright, H. PyLEnM: A machine learning framework for long-term groundwater contamination monitoring strategies. *Environ. Sci. Technol.* **2022**, *56*, 5973−5983.
(9) Zhang, T.; Lowry, G. V.; Capiro, N. L.; Chen, J.; Chen, W.; Chen, Y.; Dionysiou, D. D.; Elliott, D. W.; Ghoshal, S.; Hofmann, T.; Hsu-Kim, H.; Hughes, J.; Jiang, C.; Jiang, G.; Jing, C.; Kavanaugh, M.; Li, Q.; Liu, S.; Ma, J.; Pan, B.; Phenrat, T.; Qu, X.; Quan, X.; Saleh, N.; Vikesland, P. J.; Wang, Q.; Westerhoff, P.; Wong, M. S.; Xia, T.; Xing, B.; Yan, B.; Zhang, L.; Zhou, D.; Alvarez, P. J. J. *In situ* remediation of subsurface contamination: opportunities and challenges for nanotechnology and advanced materials. *Environ. Sci.: Nano* **2019**, *6*, 1283−1302.
(10) Martin, T. A.; Kempton, J. H. *In situ* stabilization of metal-contaminated groundwater by hydrous ferric oxide: An experimental and modeling investigation. *Environ. Sci. Technol.* **2000**, *34*, 3229−3234.
(11) Liu, W.; Zheng, J.; Ou, X.; Liu, X.; Song, Y.; Tian, C.; Rong, W.; Shi, Z.; Dang, Z.; Lin, Z. Effective extraction of Cr(VI) from hazardous gypsum sludge via controlling the phase transformation and chromium species. *Environ. Sci.: Nano* **2018**, *52*, 13336−13342.
(12) Hausladen, D. M.; Fendorf, S. Hexavalent chromium generation within naturally structured soils and sediments. *Environ. Sci. Technol.* **2017**, *51*, 2058−2067.
(13) Zhao, W.; Huang, X.; Gong, J.; Ma, L.; Qian, J. Influence of aquifer heterogeneity on Cr(VI) diffusion and removal from groundwater. *Environ. Sci. Pollut. Res.* **2022**, *29*, 3918−3929.
(14) Fruchter, J. Peer reviewed: *In-situ* treatment of chromium-contaminated groundwater. *Environ. Sci. Technol.* **2002**, *36*, 464A−472A.
(15) Ludwig, R. D.; Su, C.; Lee, T. R.; Wilkin, R. T.; Acree, S. D.; Ross, R. R.; Keeley, A. *In situ* chemical reduction of Cr (VI) in groundwater using a combination of ferrous sulfate and sodium dithionite: a field investigation. *Environ. Sci. Technol.* **2007**, *41*, 5299−5305.
(16) U. S. Environmental Protection Agency. *Permeable Reactive Barrier Technologies for Contaminant Remediation (Technical Resource Guide), EPA 600/R-98/125*; US EPA, 1998.
(17) Wang, W.; Zhang, M.; Qiu, H.; Gong, T.; Xiang, M.; Li, H. Microbe-mineral interaction-induced microorganism-augmented permeable reactive barriers for remediation of contaminated soil and groundwater: A review. *ACS ES & T Water* **2023**, *3*, 2024−2040.
(18) U. S. Environmental Protection Agency. *Groundwater Pump and Treat Systems: Summary of Selected Cost and Performance*

Information at Superfund-Financed Sites, EPA 542-R-01-021b; US EPA, 2001.
(19) Gibson, J. M.; Kavanaugh, M. C. Restoring contaminated groundwater: An achievable goal? *Environ. Sci. Technol.* **1994**, *28*, 362−368. U. S
(20) Xie, X.; Liu, Y.; Pi, K.; Liu, C.; Li, J.; Duan, M.; Wang, Y. *In situ* Fe-sulfide coating for arsenic removal under reducing conditions. *J. Hydrol.* **2016**, *534*, 42−49.
(21) Tiwari, M.; Mandal, K. K.; Raychoudhury, T. Evaluation of injection schedule for synthesizing iron-sulfide within the porous media for immobilizing arsenite: *In-situ* remediation approach for arsenic in groundwater. *Groundwater Sustainable Dev.* **2020**, *10*, 100320.
(22) Ray, J. R.; Lee, B.; Baltrusaitis, J.; Jun, Y. Formation of iron(III) (hydr)oxides on polyaspartate- and alginate-coated substrates: Effects of coating hydrophilicity and functional group. *Environ. Sci. Technol.* **2012**, *46*, 13167−13175.
(23) Dai, C.; Zuo, X.; Cao, B.; Hu, Y. Homogeneous and heterogeneous $(Fe_x, Cr_{1-x})(OH)_3$ precipitation: Implications for Cr sequestration. *Environ. Sci. Technol.* **2016**, *50*, 1741−1749.
(24) Wu, X.; Lee, B.; Jun, Y. Interfacial and activation energies of environmentally abundant heterogeneously nucleated iron(III) (hydr)oxide on quartz. *Environ. Sci. Technol.* **2020**, *54*, 12119−12129.
(25) Zhang, Z.; Si, R.; Lv, J.; Ji, Y.; Chen, W.; Guan, W.; Cui, Y.; Zhang, T. Effects of extracellular polymeric substances on the formation and methylation of mercury sulfide nanoparticles. *Environ. Sci. Technol.* **2020**, *54*, 8061−8071.
(26) Liu, Y.; Gan, H.; Tian, L.; Liu, Z.; Ji, Y.; Zhang, T.; Alvarez, P. J. J.; Chen, W. Partial oxidation of FeS nanoparticles enhances Cr(VI) sequestration. *Environ. Sci. Technol.* **2022**, *56*, 13954−13963.
(27) Patterson, R. R.; Fendorf, S.; Fendorf, M. Reduction of hexavalent chromium by amorphous iron sulfide. *Environ. Sci. Technol.* **1997**, *31*, 2039−2044.
(28) Gong, Y.; Tang, J.; Zhao, D. Application of iron sulfide particles for groundwater and soil remediation: A review. *Water Res.* **2016**, *89*, 309−320.
(29) Lyu, H. H.; Tang, J. C.; Huang, Y.; Gai, L. S.; Zeng, E. Y.; Liber, K.; Gong, Y. Y. Removal of hexavalent chromium from aqueous solutions by a novel biochar supported nanoscale iron sulfide composite. *Chem. Eng. J.* **2017**, *322*, 516−524.
(30) Liao, P.; Pan, C.; Ding, W. Y.; Li, W. L.; Yuan, S. H.; Fortner, J. D.; Giammar, D. E. Formation and transport of Cr(III)-NOM-Fe colloids upon reaction of Cr(VI) with NOM-Fe(II) colloids at anoxic-oxic interfaces. *Environ. Sci. Technol.* **2020**, *54*, 4256−4266.
(31) Hu, Y.; Lee, B.; Bell, C.; Jun, Y. Environmentally abundant anions influence the nucleation, growth, ostwald ripening, and aggregation of hydrous Fe(III) Oxides. *Langmuir* **2012**, *28*, 7737−7746.
(32) Scheidegger, A.; Borkovec, M.; Sticher, H. Coating of silica sand with goethite: preparation and analytical identification. *Geoderma* **1993**, *58*, 43−65.
(33) Xu, Y.; Axe, L. Synthesis and characterization of iron oxide-coated silica and its effect on metal adsorption. *J. Colloid Interface Sci.* **2005**, *282*, 11−19.
(34) Daugherty, E.; Gilbert, B.; Nico, P.; Borch, T. Complexation and redox buffering of iron(II) by dissolved organic matter. *Environ. Sci. Technol.* **2017**, *51*, 11096−11104.
(35) Qu, X.; Fu, H.; Mao, J.; Ran, Y.; Zhang, D.; Zhu, D. Chemical and structural properties of dissolved black carbon released from biochars. *Carbon* **2016**, *96*, 759−767.
(36) Chen, W.; Westerhoff, P.; Leenheer, J. A.; Booksh, K. Fluorescence excitation-emission matrix regional integration to quantify spectra for dissolved organic matter. *Environ. Sci. Technol.* **2003**, *37*, 5701−5710.
(37) Shen, Z.; Zhang, Z.; Li, T.; Yao, Q.; Zhang, T.; Chen, W. Facet-dependent adsorption and fractionation of natural organic matter on crystalline metal oxide nanoparticles. *Environ. Sci. Technol.* **2020**, *54*, 8622−8631.
(38) Dai, C.; Hu, Y. Fe(III) hydroxide nucleation and growth on quartz in the presence of Cu(II), Pb(II), and Cr(III): Metal hydrolysis and adsorption. *Environ. Sci. Technol.* **2015**, *49*, 292−300.
(39) Li, Q.; Fernandez-Martinez, A.; Lee, B.; Waychunas, G. A.; Jun, Y. Interfacial energies for heterogeneous nucleation of calcium carbonate on mica and quartz. *Environ. Sci. Technol.* **2014**, *48*, 5745−5753.
(40) Li, T.; Senesi, A. J.; Lee, B. Small angle X-ray scattering for nanoparticle research. *Chem. Rev.* **2016**, *116* (18), 11128−11180.
(41) Thanh, N. T. K.; Maclean, N.; Mahiddine, S. Mechanisms of nucleation and growth of nanoparticles in solution. *Chem. Rev.* **2014**, *114*, 7610−7630.
(42) Wu, X.; Bowers, B.; Kim, D.; Lee, B.; Jun, Y. Dissolved organic matter affects arsenic mobility and iron(III) (hydr)oxide formation: Implications for managed aquifer recharge. *Environ. Sci. Technol.* **2019**, *53*, 14357−14367.
(43) Lin, M. M.; Kim, D. K.; El Haj, A. J.; Dobson, J. Development of superparamagnetic iron oxide nanoparticles (SPIONS) for translation to clinical applications. *IEEE Trans. Nanobiosci.* **2008**, *7*, 298−305.
(44) Deng, N.; Stack, A. G.; Weber, J.; Cao, B.; De Yoreo, J. J.; Hu, Y. Organic-mineral interfacial chemistry drives heterogeneous nucleation of Sr-rich $(Ba_x, Sr_{1-x})SO_4$ from undersaturated solution. *Proc. Natl. Acad. Sci. U.S.A.* **2019**, *116*, 13221−13226.
(45) Hu, Y.; Neil, C.; Lee, B.; Jun, Y. Control of heterogeneous Fe(III) (hydr)oxide nucleation and growth by interfacial energies and local saturations. *Environ. Sci. Technol.* **2013**, *47*, 9198−9206.
(46) Dai, C.; Stack, A. G.; Koishi, A.; Fernandez-Martinez, A.; Lee, S. S.; Hu, Y. Heterogeneous nucleation and growth of barium sulfate at organic-water interfaces: Interplay between surface hydrophobicity and Ba^{2+} adsorption. *Langmuir* **2016**, *32*, 5277−5284.
(47) Zhang, S.; Cheng, L.; Zuo, X.; Cai, D.; Tong, K.; Hu, Y.; Ni, J. $(Fe, Cr)(OH)_3$ coprecipitation in solution and on soil: Roles of surface functional groups and solution pH. *Environ. Sci. Technol.* **2023**, *57*, 7516−7525.
(48) Huangfu, X.; Jiang, J.; Ma, J.; Liu, Y.; Yang, J. Aggregation kinetics of manganese dioxide colloids in aqueous solution: Influence of humic substances and biomacromolecules. *Environ. Sci. Technol.* **2013**, *47*, 10285−10292.
(49) Louie, S. M.; Tilton, R. D.; Lowry, G. V. Effects of molecular weight distribution and chemical properties of natural organic matter on gold nanoparticle aggregation. *Environ. Sci. Technol.* **2013**, *47*, 4245−4254.
(50) Furman, O.; Usenko, S.; Lau, B. L. T. Relative importance of the humic and fulvic fractions of natural organic matter in the aggregation and deposition of silver nanoparticles. *Environ. Sci. Technol.* **2013**, *47*, 1349−1356.
(51) Suzuki, T.; Kawai, K.; Moribe, M.; Niinae, M. Recovery of Cr as Cr(III) from Cr(VI)-contaminated kaolinite clay by electrokinetics coupled with a permeable reactive barrier. *J. Hazard. Mater.* **2014**, *278*, 297−303.
(52) Jun, Y.; Kim, D.; Neil, C. W. Heterogeneous nucleation and growth of nanoparticles at environmental interfaces. *Acc. Chem. Res.* **2016**, *49*, 1681−1690.
(53) Li, W.; Liao, P.; Oldham, T.; Jiang, Y.; Pan, C.; Yuan, S.; Fortner, J. D. Real-time evaluation of natural organic matter deposition processes onto model environmental surfaces. *Water Res.* **2018**, *129*, 231−239.
(54) Saleh, N.; Kim, H.; Phenrat, T.; Matyjaszewski, K.; Tilton, R. D.; Lowry, G. V. Ionic strength and composition affect the mobility of surface-modified Fe^0 nanoparticles in water-saturated sand columns. *Environ. Sci. Technol.* **2008**, *42*, 3349−3355.
(55) Huangfu, X.; Ma, C.; Huang, R.; He, Q.; Liu, C.; Zhou, J.; Jiang, J.; Ma, J.; Zhu, Y.; Huang, M. Deposition kinetics of colloidal manganese dioxide onto representative surfaces in aquatic environments: The role of humic acid and biomacromolecules. *Environ. Sci. Technol.* **2019**, *53*, 146−156.
(56) Hook, F.; Kasemo, B.; Nylander, T.; Fant, C.; Sott, K.; Elwing, H. Variations in coupled water, viscoelastic properties, and film

https://doi.org/10.1021/acs.est.3c10637
Environ. Sci. Technol. 2024, 58, 7186−7195

thickness of a Mefp-1 protein film during adsorption and cross-linking: A quartz crystal microbalance with dissipation monitoring, ellipsometry, and surface plasmon resonance study. *Anal. Chem.* **2001**, *73*, 5796−5804.

https://doi.org/10.1021/acs.est.3c10637
Environ. Sci. Technol. 2024, 58, 7186−7195